Supplementary Materials for

Fully Tunable On-Chip Meta-Generator for Multidimensional Poincaré Sphere mapping

Jing Luan[1,2,+], Tiange Wu[1,2,+], Shuang Zheng[1,2,*], Zhenyu Wan[1], Yuan Meng[4], Yijie Shen[3,5], Kaiyuan Wang[1,2], Deming Liu[1,2], Jian Wang[1,*] and Minming Zhang[1,2,*]

[1]*School of Optical and Electronic Information and Wuhan National Laboratory for Optoelectronics, Huazhong University of Science and Technology, Wuhan 430074, Hubei, China*

[2]*National Engineering Research Center for Next Generation Internet Access System, Wuhan, Hubei 430074, China*

[3]*Centre for Disruptive Photonic Technologies, School of Physical and Mathematical Sciences & The Photonics Institute, Nanyang Technological University, Singapore 637371, Singapore*

[4]*Mechanical Engineering and Materials Science, Washington University in St Louis, St Louis, MO, 63130, USA*

[5]*School of Electrical and Electronic Engineering, Nanyang Technological University, Singapore 639798, Singapore*

* *zshust@hust.edu.cn, jwang@hust.edu.cn, and mmz@hust.edu.cn*

Section S1. Details of simulation and optimization process

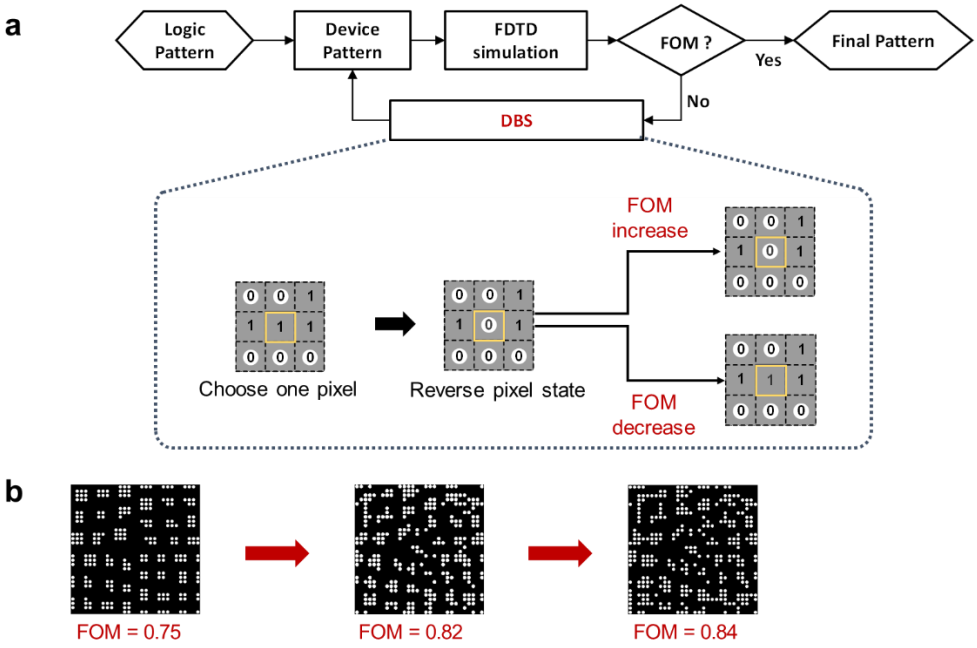

Fig. S1. Schematic of simulation and optimization process. a. Flow chart for the optimization process. **b**. The optimized 2D pixel array pattern and corresponding FOM.

The 3D FDTD simulations assisted with improved direct-binary-search (DBS) algorithm are performed to design optimum pattern in Fig. S1(a). We first toggle the logical state of one pixel to calculate the initial FOM. Then, the pixel state is retained once the FOM is improved, if not, the pixel will be toggled to the original state. One iteration could traverse all the pixels and the whole optimization will end up with the FOM exhibiting no greater improvement after several iterations (5% for our case). It takes about 168 *h* to obtain the optimized pixel array of the meta-waveguide after two rounds of iteration, on the workstation with a twenty-core central processing unit (Intel Core i9-10900X). Figure S1(b) indicates the 2D pixel array pattern and calculated FOM of initial structure, first iteration and second iteration, respectively. As can be seen, the FOM increases from the 0.75 to 0.84.

Section S2. Simulation of initial structures

Figure S3(a) presents the electric field intensity, phase distribution, and collinear interferograms of the eight OAM modes generated by the initial PhC-like structure array before optimization at 1550 nm. The field intensity profiles reveal incomplete annular structures, indicating deviations from ideal vortex beams. Notably, the phase singularities of the OAM_{-2} and OAM_{+2} modes appear at two distinct locations,

exhibiting discontinuous phase features. Similar characteristics are observed for all eight OAM modes in Figure S3(b). These results confirm that the initial structure exhibits significantly degraded vortex beam properties compared to the optimized design, underscoring the effectiveness of the inverse design approach in achieving high-purity OAM generation.

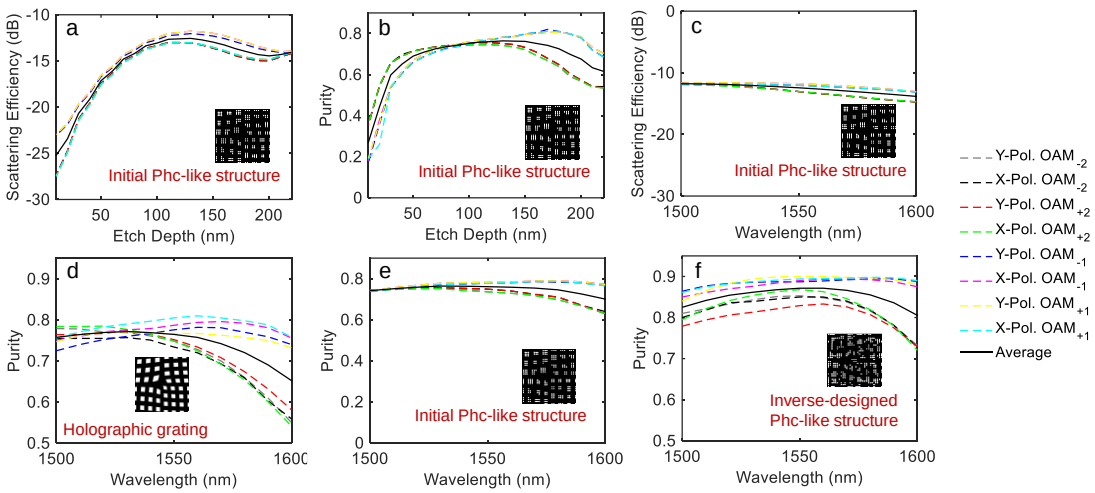

Fig. S2. Simulated scattering efficiency and purity. a-f. Simulated scattering efficiency and purity for 2D meta-waveguide.

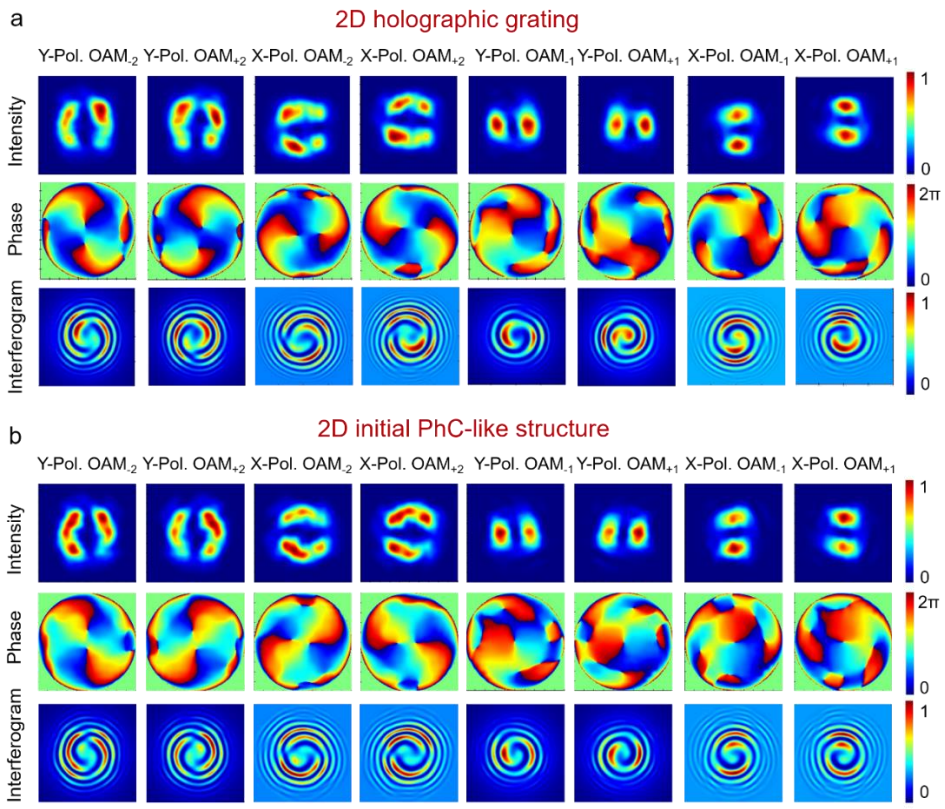

Fig. S3. Simulated intensity profiles, phase distributions, and interferograms for (a) 2D holographic grating and (b) 2D initial PhC-like structure.

Section S3. Evolution process of in-plane guided mode to out-plane OAM mode

To investigate the evolution process of in-plane guided mode to out-plane OAM mode, we simulate the electrical field distributions of the yellow square region (width = 6 μm) in Fig. S4 (including waveguide region and grating region) at different height (z = 0.2, 0.4, 0.6, 0.8, 1.0 μm, far field). z = 0 represents the bottom of the silicon core layer. Figure S6 indicates the real part distributions of the electric field components of 8 OAM modes for 2D meta-waveguide (y-Pol. OAM_{-2}, x-Pol. OAM_{-2}, y-Pol. OAM_{+2}, x-Pol. OAM_{+2}, y-Pol. OAM_{-1}, x-Pol. OAM_{-1}, y-Pol. OAM_{+1} and x-Pol. OAM_{+1}), respectively. We can observe the mode evolution from the guided mode to free space mode based on the electric field distributions of different height.

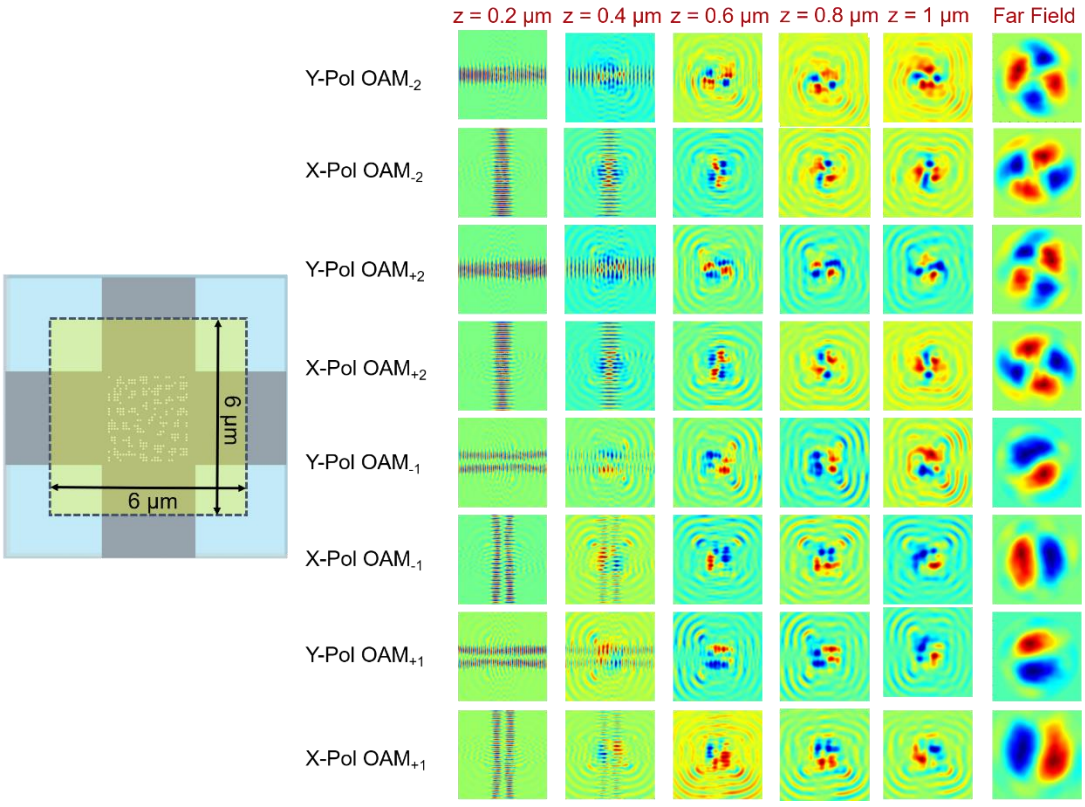

Fig. S4. Simulation results for the evolution process of in-plane guided modes (TE_0 and TE_1) to out-plane OAM modes.

Section S4. The mapping relationship between waveguide modes and structured light beams (OAM, LP, and vector modes)

Based on the OAM mode basis enabled by the proposed 2D meta-waveguide, on-chip multiple guided modes can be further mapped to more complex structured beams, including arbitrarily polarized OAM modes on conventional Poincaré spheres (PSs), linearly-polarized (LP) modes on OAM PSs, and cylindrical vector (CV) modes on higher-order Poincaré spheres (HOPSs). By

controlling the amplitude and phase of the guided modes, arbitrary structured light beams could be generated by the proposed device. For example, LP modes on OAM orbit could be generated by combining two OAM modes with same polarization and opposite topological charges. The vector modes on HOPSs could be generated by combining left- and right-circularly polarized OAM modes with both opposite spin polarizations and topological charges.

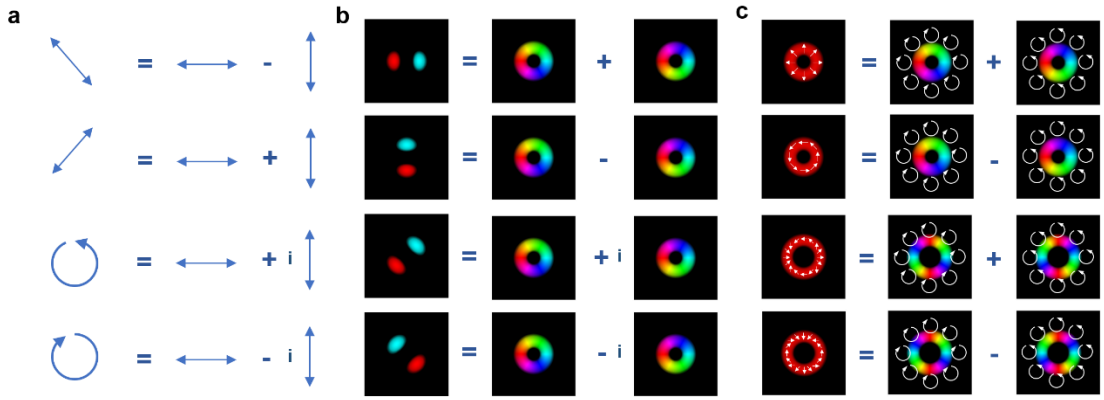

Fig. S5. Decompositions of (a) various polarization states on polarization PS and (b) LP modes on OAM PS in terms of orthogonal linear polarization states and orthogonal OAM modes, respectively. (c) Decomposition of vector modes on HOPSs in terms of orthogonal OAM modes. The color change indicates the relative phase of the components. Arrows indicate polarization direction.

Table S1. Mapping of 2D PIC guides modes to OAM, LP, and vector modes

PIC modes		Port 2 +x TE_0	Port 1 -x TE_0	Port 2 +x TE_1	Port 1 -x TE_1	Port 4 +y TE_0	Port 3 -y TE_0	Port 4 +y TE_1	Port 3 -y TE_1
OAM modes		y-Pol. OAM_{+2}	y-Pol. OAM_{-2}	y-Pol. OAM_{+1}	y-Pol. OAM_{-1}	x-Pol. OAM_{+2}	x-Pol. OAM_{-2}	x-Pol. OAM_{+1}	x-Pol. OAM_{-1}
LP modes on OAM PSs	LP^{o}_{21y}	1	1						
	LP^{e}_{21y}	1	-1						
	LP^{o}_{11y}			1	1				
	LP^{e}_{11y}			1	-1				
	LP^{e}_{21x}					1	1		
	LP^{o}_{21x}					1	-1		
	LP^{e}_{11x}							1	1
	LP^{o}_{11x}							1	-1
Vector modes on HOPSs	m=1, $\varphi_0=0$			-1	1			-1	1
	m=1, $\varphi_0=\pi/4$			-i	1			-i	1
	m=1, $\varphi_0=\pi/2$			1	1			1	1
	m=1, $\varphi_0=3\pi/4$			1	-i			1	-i
	m=2, $\varphi_0=0$	i	-i			1	1		
	m=2, $\varphi_0=\pi/4$	-i	1			-1	i		
	m=2, $\varphi_0=\pi/2$	1	1			-i	i		
	m=2, $\varphi_0=3\pi/4$	i	1			1	i		

Vector modes on HOPSs	m=-1, φ_0=0			1	-1			-1	1
	m=-1, φ_0=π/4			1	-i			-1	i
	m=-1, φ_0=π/2			1	1			-1	-1
	m=-1, φ_0=3π/4			1	i			-1	-i
	m=-2, φ_0=0	-i	i			1	1		
	m=-2, φ_0=π/4	-i	-1			1	i		
	m=-2, φ_0=π/2	-i	-i			1	-1		
	m=-2, φ_0=3π/4	-i	1			1	-i		

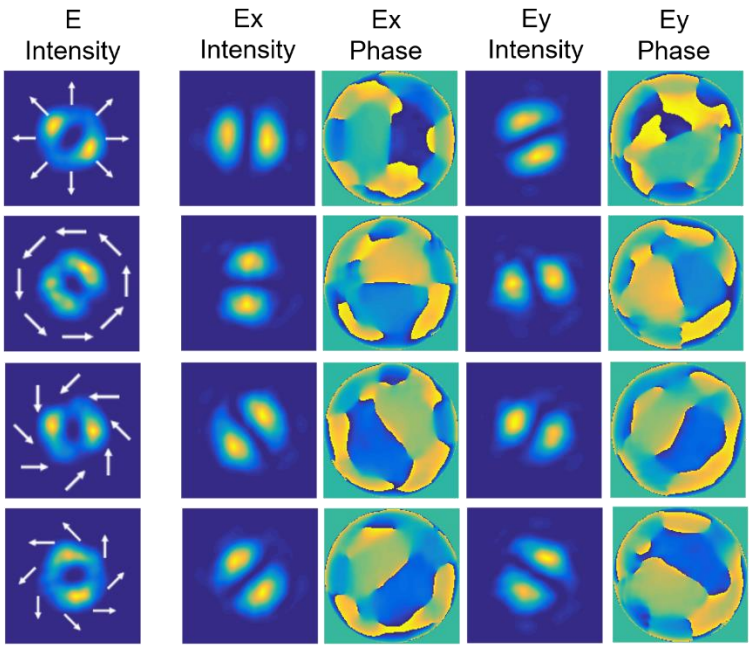

Fig. S6. Simulation results for the generation of first-order CV beams mapped on HOPS.

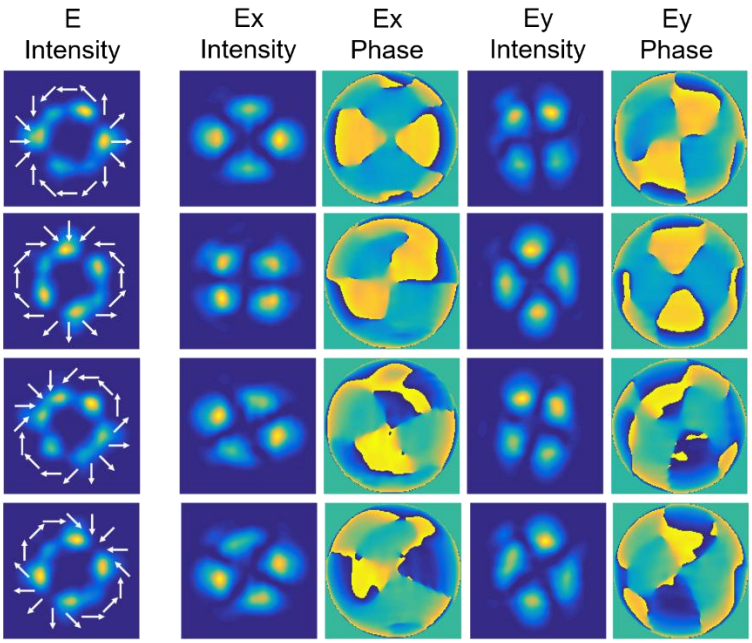

Fig. S7. Simulation results for the generation of second-order CV beams mapped on HOPS.

Section S5. Device fabrication process

As indicates in Fig. S8, the two optimized ultra-compact OAM emitters based on PhC-like SWG structures were fabricated and experimentally demonstrated on standard silicon-on-insulator (SOI) wafer. We use an electron beam lithography system (Vistec EBPG 5000 Plus) to form the optimized pattern on SOI platform with a 220 nm thick top silicon layer and an inductively coupled plasma etcher (Plasma lab System100) to transfer the mask to the silicon device layer. The pixel-array is approximately etched up to 130 nm by setting the proper etching time, while the waveguides outlines are fully etched down 220 nm to the buried oxide. A 2-μm-thick SiO_2 layer is deposited on the silicon layer by plasma-enhanced chemical vapor deposition (PlasmaPro 800 Stratum PECVD).

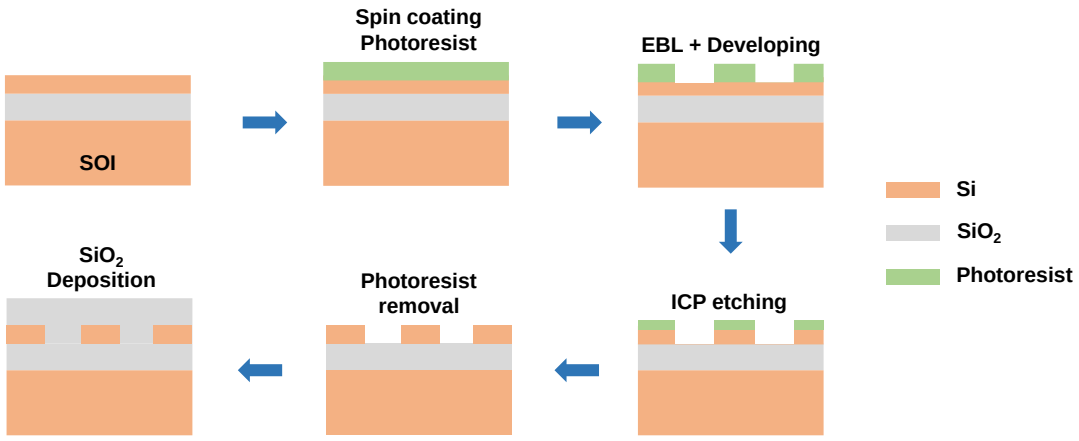

Fig. S8. Illustration of the device fabrication process of the devices (spin coating, electron-beam lithography, inductively coupled plasma, photoresist removal, and PECVD upper SiO_2 cladding).

Section S6. Experiment results of the other channels

Figure S9(a) shows the measured far-field intensity, coaxial and tilt interferograms of six OAM modes for 2D meta-waveguide (y-Pol. OAM_{-2}, y-Pol. OAM_{+2}, x-Pol. OAM_{+2}, y-Pol. OAM_{-1}, x-Pol. OAM_{-1}, and x-Pol. OAM_{+1}) at 1530, 1550 and 1565 nm. Doughnut shaped intensity profiles and spiral interference patterns verify the helical phase front of the generated OAM modes. Topological charge order can be recognized by the number of spiral arms and the spiral direction in the interferograms. Fork structures at the tilt interferograms beam also verify the successful generation of broadband vortex beams. Figure S10 shows that when the polarization changes from 0° to 90°, the power of x-Pol. OAM_{-2} mode increases gradually from the maximum to the minimum, while the opposite trend for the power of y-Pol. OAM_{+1} mode.

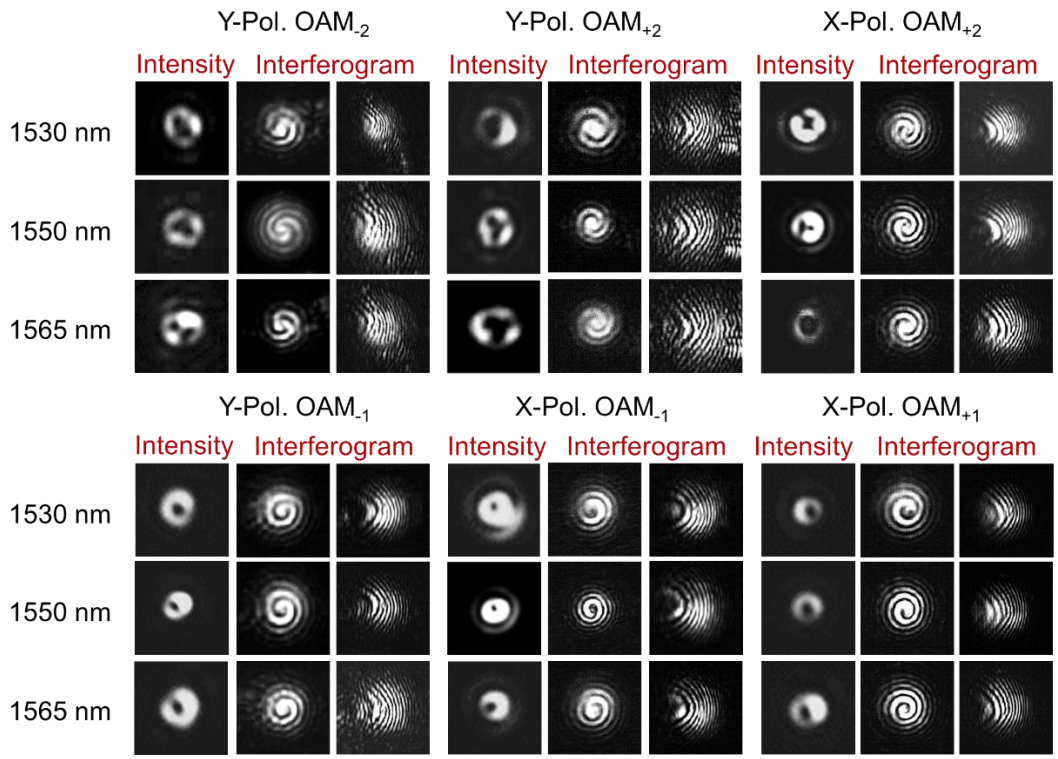

Fig. S9. Measured additional results for broadband vortex beam generation with the meta-waveguide.

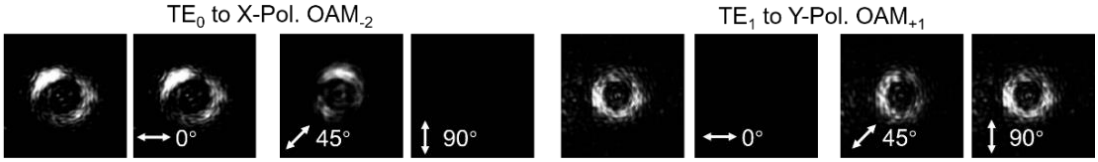

Fig. S10. Measured results for the verification of the emission light polarization state.

Section S7. Experiment results of OAM mode demodulation

As shown in Fig. S14, the emitted OAM modes of the fabricated 1D meta-waveguide can be demodulated to a bright spot at the beam center (Gaussian-like beam) when meeting an inverse phase pattern, while remains the doughnut field profile with another topological charge in the case of non-corresponding demodulation phase pattern. Meanwhile, the orthogonal component of the detecting mode appears weak light. Similarly, the demodulated performance of 2D meta-waveguide is clearly characterized in Fig. S14(b), with corresponding Gaussian-like points in the diagonal elements.

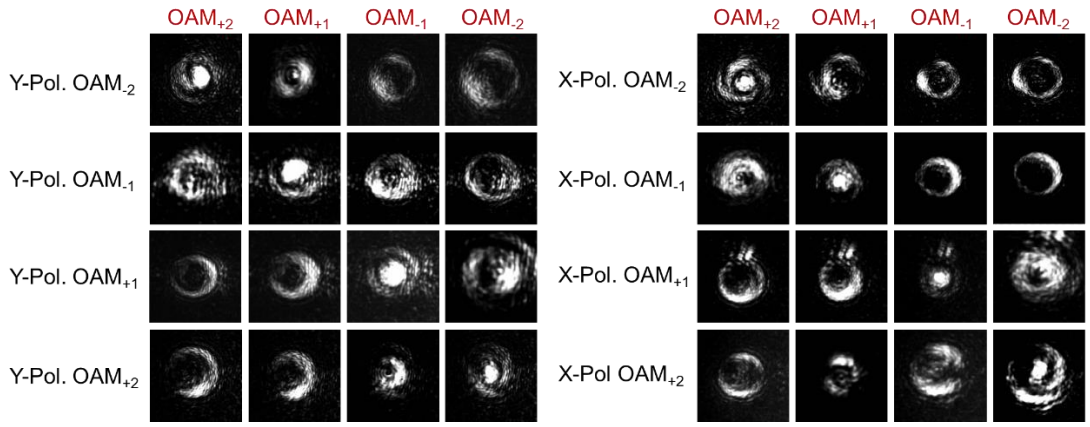

Fig. S11. Measured results for eight OAM modes demodulation.

Section S8. Numerical analysis of the fabrication tolerance

To investigate the fabrication tolerance of the OAM emitters, we here change the radii of etching hole from 40 to 50 nm and simulate the performance of OAM modes. Figure. S15 shows the simulated average purity of 2D meta-waveguide's 8 modes and 1D meta-waveguide's 4 modes as a function of radii at the center wavelength of 1550 nm, respectively. Specifically, in the whole range of ±5 nm variation, the fluctuations of average purity can be limited to negligible values as 0.014 and 0.016 for both meta-waveguides, which show perfect robustness and fabrication tolerance.

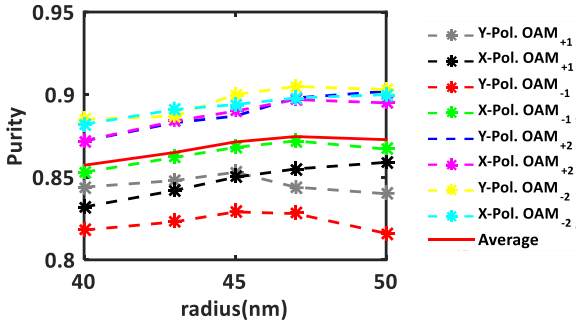

Fig. S12. Numerical analysis of the fabrication tolerance. Simulated results for 2D meta-waveguide.

Section S9. Experimental Configuration

The measurement setup shown in Figure. S13 is used to characterized the performance of OAM emitters. The light from a tunable light source with the wavelength from 1530 to 1565 nm was split into two branches by a 3-dB coupler. One branch was attenuated to the appropriate power and collimated to produce the reference Gaussian beam. A polarizer and a half wave plate (HWP) were used to ensure a

consistent polarization between the emission beam and the reference beam. The other branch passed through polarization controller (PC) and was coupled into the chip by a lensed fiber. The generated polarization and order diversity OAM mode was collimated by an objective lens (10×, NA= 0.26). The beam size and polarization can be adjusted by polarizer, half wave plate (HWP) and lens. The intensity profiles of the generated OAM modes and their interference patterns with the reference Gaussian beams were monitored with an infrared CCD camera (Xenics, Bobcat-640-GigE). The other branch of OAM separated by the beam splitter was demodulated to Gaussian-like beam by a spatial light modulator (SLM, Meadowlark Optics E19×12). One branch of the demodulated beam was captured by the infrared CCD camera to get the field intensity. The other branch was coupled into a single mode fiber connected with the power meter to measure the optical power.

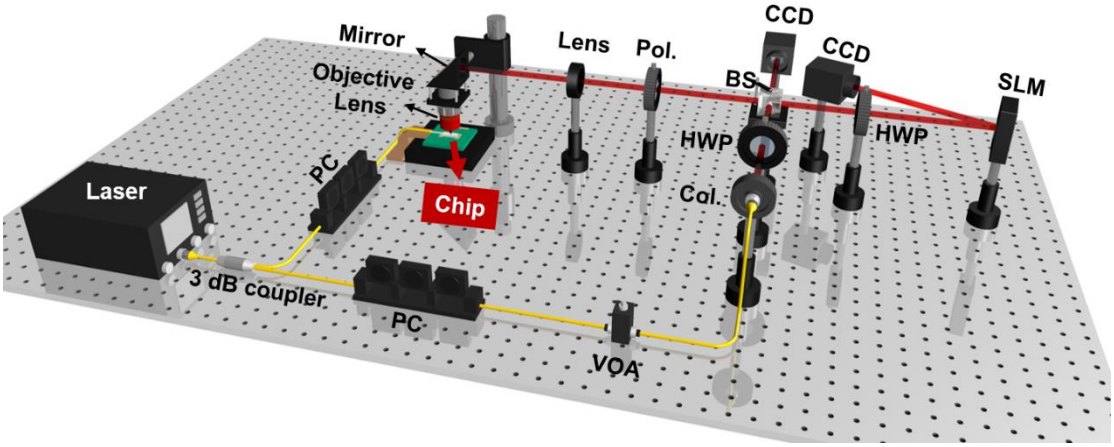

Fig. S13. Experimental setup. PC, polarization controller; VOA, variable optical attenuator; Col., collimator; Pol., polarizer; HWP, half-wave plate; BS, beam splitter; SLM: spatial light modulator.

Section S10. A comparison of on-chip structured light beam generators

Table S2. A comparison of on-chip structured light beam generators

Table 1. A comparison of on-chip structured light beam generators

No.	Citations	Principle	Number of multiplexed guided mode	Number of basis mode	Tunable dimensions of basis modes	Number of generated PS beams	Switch speed (μs)	On-chip tuning
1	Light.: Sci. Appl. 7, 18001 (2018).	Subwavelength structure	**2**	**2**	**-**	**2**	-	✗
2	Sci. Adv. 5, eaau9593 (2019).	Holographic grating	**4**	**4**	**-**	**4**	-	✗
3	ACS Photonics, **10**, 803–807 (2023).	Meta-waveguide	**3**	**3**	**-**	**3**	-	✗
4	Nano Lett. 23 (7), 750-2757 (2023).	Meta-waveguide	**2**	**2**	**-**	CV modes	-	✗
5	Nat. Photon. 18, 243–249 (2024).	Reconfigurable PIC + Grating array	**1**	-	Amplitude and phase	Phase-structured light beams	**~10**	✓
6	Nature 612, 246–251 (2022).	Two coupled microlasers	**4**	**4**	Amplitude and phase	2 Poincaré spheres	**-**	✓
This work		**Reconfigurable PIC + Multimode meta-waveguide**	**8**	**8**	**Full dimensions (Amplitude, phase, polarization and topological charge)**	**All states across > 8 Poincaré spheres**	**~10**	✓